

See discussions, stats, and author profiles for this publication at: <https://www.researchgate.net/publication/273463671>

# Multifunctional Dendrimer–Entrapped Gold Nanoparticles Modified with RGD Peptide for Targeted CT/MR Dual Modal Imaging of Tumors.

ARTICLE in ANALYTICAL CHEMISTRY · MARCH 2015

Impact Factor: 5.64 · DOI: 10.1021/acs.analchem.5b00135 · Source: PubMed

CITATIONS

5

READS

35

8 AUTHORS, INCLUDING:



Han Wang

Shanghai Jiao Tong University

32 PUBLICATIONS 680 CITATIONS

SEE PROFILE



Shihui Wen

Donghua University

37 PUBLICATIONS 694 CITATIONS

SEE PROFILE



Guixiang Zhang

Shanghai Jiao Tong University

101 PUBLICATIONS 1,670 CITATIONS

SEE PROFILE



Xiangyang Shi

Donghua University

219 PUBLICATIONS 7,066 CITATIONS

SEE PROFILE

# Multifunctional Dendrimer-Entrapped Gold Nanoparticles Modified with RGD Peptide for Targeted Computed Tomography/Magnetic Resonance Dual-Modal Imaging of Tumors

Qian Chen,<sup>†,‡</sup> Han Wang,<sup>§,‡</sup> Hui Liu,<sup>‡</sup> Shihui Wen,<sup>‡</sup> Chen Peng,<sup>||</sup> Mingwu Shen,<sup>\*,‡</sup> Guixiang Zhang,<sup>\*,§</sup> and Xiangyang Shi<sup>\*,†,‡,⊥</sup>

<sup>†</sup>State Key Laboratory for Modification of Chemical Fibers and Polymer Materials, College of Materials Science and Engineering, and

<sup>‡</sup>College of Chemistry, Chemical Engineering and Biotechnology, Donghua University, Shanghai 201620, People's Republic of China

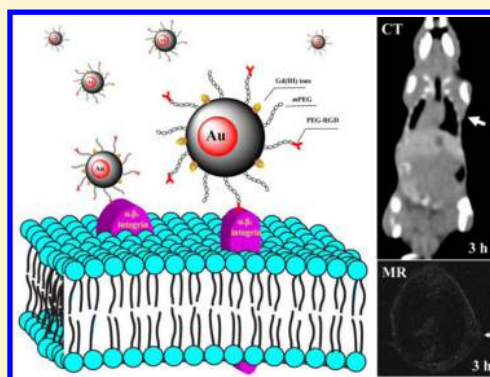
<sup>§</sup>Department of Radiology, Shanghai First People's Hospital, School of Medicine, Shanghai Jiaotong University, Shanghai 200080, People's Republic of China

<sup>||</sup>Department of Radiology, School of Medicine, Shanghai Tenth People's Hospital Affiliated with Tongji University, Shanghai 200072, People's Republic of China

<sup>⊥</sup>CQM-Centro de Química da Madeira, Universidade da Madeira, Campus da Penteada, 9000-390 Funchal, Portugal

## S Supporting Information

**ABSTRACT:** We report the use of multifunctional dendrimer-entrapped gold nanoparticles (Au DENPs) loaded with gadolinium (Gd) chelator/Gd(III) complexes and surface-modified with thiolated cyclo(Arg-Gly-Asp-Phe-Lys-mpa) (RGD) peptide for targeted dual-mode computed tomography (CT)/magnetic resonance (MR) imaging of small tumors. In this study, amine-terminated generation 5 poly(amidoamine) dendrimers were used as a nanopatform to be covalently modified with Gd chelator, RGD via a polyethylene glycol (PEG) spacer, and PEG monomethyl ether. Then the multifunctional dendrimers were used as templates to entrap gold nanoparticles, followed by chelating Gd(III) ions and acetylation of the remaining dendrimer terminal amines. The thus-formed multifunctional Au DENPs (in short, Gd–Au DENPs-RGD) were characterized via different techniques. We show that the multifunctional Au DENPs with a Au core size of 3.8 nm are water-dispersible, stable under different pH (5–8) and temperature conditions (4–50 °C), and noncytotoxic at a Au concentration up to 100  $\mu$ M. With the displayed X-ray attenuation property and the  $r_1$  relaxivity ( $2.643 \text{ mM}^{-1} \text{ s}^{-1}$ ), the developed Gd–Au DENPs-RGD are able to be used as a dual-mode nanoprobe for targeted CT/MR imaging of an  $\alpha_v\beta_3$  integrin-overexpressing xenografted small tumor model in vivo via RGD-mediated active targeting pathway. The developed multifunctional Gd–Au DENPs-RGD may be used as a promising dual-mode nanoprobe for targeted CT/MR imaging of different types of  $\alpha_v\beta_3$  integrin-overexpressing cancer.



Molecular imaging has been identified as an effective strategy for early-stage diagnosis of cancer. Due to the drawbacks of conventional small molecular contrast agents such as short imaging time, renal toxicity at a relatively high concentration, and lack of specificity,<sup>1</sup> it is essential to develop various novel contrast agents to overcome these shortcomings. The advances in nanotechnology make it possible to develop various nanoparticulate contrast agents for different molecular imaging applications.<sup>2–4</sup> Among the different imaging modalities employed, computed tomography (CT) has been appealing since it provides high spatial and density resolution and valuable 3-dimensional (3D) tomography information on the anatomic structure based on the differential X-ray absorptions between the tissues and lesions.<sup>5,6</sup> Various nanoparticulate contrast agents such as Au,<sup>7–11</sup> Bi<sub>2</sub>S<sub>3</sub>,<sup>12,13</sup> TaO<sub>x</sub> ( $x \approx 1$ ),<sup>14</sup> and NaGdF<sub>4</sub><sup>15</sup> nanoparticles (NPs) have been explored as new CT contrast agents. On the other hand,

magnetic resonance (MR) imaging has been extensively used as a powerful technique in clinical diagnosis due to its superior resolution and tomographic capabilities.<sup>16–18</sup> Two major types of MR contrast agents, gadolinium (Gd<sup>3+</sup>)-based  $T_1$  contrast agents<sup>19,20</sup> and the superparamagnetic iron oxide NP-based  $T_2$  contrast agents,<sup>21–23</sup> have been developed.

Due to the fact that each imaging modality has its own advantages and disadvantages, it is important to incorporate two different types of imaging elements within a single nanoparticulate system, enabling dual-mode CT/MR imaging applications.<sup>6,24–29</sup> Different types of NPs, such as Fe<sub>3</sub>O<sub>4</sub>/TaO<sub>x</sub> core/shell NPs,<sup>26</sup> water-soluble FePt NPs,<sup>24</sup> gadolinium (Gd)-

Received: December 31, 2014

Accepted: March 13, 2015

Published: March 13, 2015



chelated Au NPs,<sup>30,31</sup> Gd-G8 dendrimers,<sup>32</sup> Fe<sub>3</sub>O<sub>4</sub>@dye-hybrid@Au NPs,<sup>33</sup> and multifunctional core/satellite particles having silica-coated rare-earth upconversion NPs as cores and ultrasmall CuS NPs as satellites,<sup>34</sup> have been developed for dual-mode CT/MR imaging applications. For tumor imaging applications, most of these NP-based contrast agents have been used only via passive targeting based on the enhanced permeability and retention (EPR) effect. It is quite challenging to develop ligand-modified multifunctional NP systems for more effective targeted dual-mode CT/MR imaging of tumors.

In our previous work, we developed a dendrimer-based nanoplatform that is able to entrap Au NPs within the dendrimer interior and load Gd(III) ions via the conjugated Gd chelator on the dendrimer periphery. The formed Gd(III)-loaded dendrimer-entrapped Au NPs (Gd–Au DENPs) are able to be used as a contrast agent for dual-mode CT/MR imaging of animal organs due to the coexistence of Au NPs (for CT imaging) and Gd(III) ions (for T<sub>1</sub>-weighted MR imaging).<sup>35</sup> Through the versatile dendrimer nanotechnology and polyethylene glycol (PEG) conjugation chemistry, multifunctional Gd–Au DENPs modified with targeting ligand folic acid (FA) can be further formed for targeted imaging of FA receptor-overexpressing tumors.<sup>6</sup> These prior successes highlight the importance of using dendrimers as a versatile nanoplatform to construct a multifunctional nanoprobe for targeted dual-mode CT/MR imaging of tumors. We therefore hypothesize that other types of tumor-targeting ligands may also be able to be linked onto the dendrimer periphery, thereby expanding the dendrimer-based nanotechnology to develop different types of nanoprobes for targeted dual-mode CT/MR imaging of different types of tumors.

Arginine-glycine-aspartic acid (Arg-Gly-Asp, RGD) peptide has been identified to be a promising targeting ligand that can specifically target cancer cells overexpressing  $\alpha_v\beta_3$  integrin.<sup>36</sup> It is known that dendrimers modified with RGD peptide can be used as a specific carrier or vector for targeted drug delivery<sup>37</sup> or gene delivery<sup>38</sup> to integrin  $\alpha_v\beta_3$ -overexpressing cancer cells, respectively. In the present study, Gd–Au DENPs modified with RGD peptide were synthesized and characterized for targeted dual-mode CT/MR imaging of integrin  $\alpha_v\beta_3$ -overexpressing tumors. First, amine-terminated generation 5 (G5) poly(amidoamine) (PAMAM) dendrimers (G5-NH<sub>2</sub>) were modified with Gd chelator, RGD via a PEG spacer, and PEG monomethyl ether (mPEG). Then the functionalized dendrimers were used as templates to entrap Au NPs and to chelate Gd(III) ions, followed by acetylation of the remaining dendrimer terminal amines to form the RGD-modified Gd–Au DENPs (for short, Gd–Au DENPs-RGD; Figure 1). The

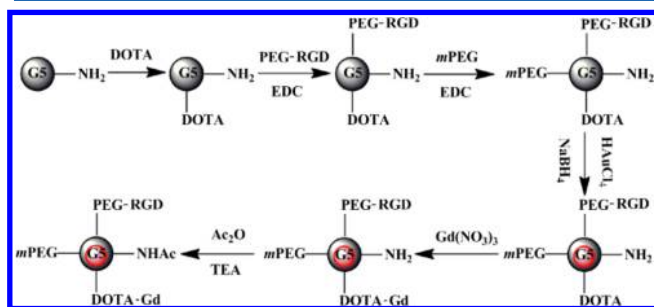


**Figure 1.** Schematic illustration of the preparation of the Gd–Au DENPs-RGD probe. Ac<sub>2</sub>O and TEA represent acetic anhydride and triethylamine, respectively.

formed Gd–Au DENPs-RGD probe was characterized via different techniques. Cytotoxicity assay, cell morphology observation, and hemolytic assay were used to evaluate the cytocompatibility and hemocompatibility of the particles. Finally, the formed Gd–Au DENPs-RGD probe was used for dual-mode targeted CT/MR imaging of a small xenografted human glioblastoma tumor model overexpressing  $\alpha_v\beta_3$  integrin. To our knowledge, this is the first paper related to the development of an RGD-targeted dendrimer-based nanoprobe for targeted dual-mode CT/MR imaging of tumors.

## EXPERIMENTAL SECTION

**Materials.** All chemicals and materials were acquired from commercial resources without further purification. U87MG cells (an  $\alpha_v\beta_3$  integrin-overexpressing human glioblastoma cell line) and L1210 cells (a mouse lymphocytic leukemia cell line) were obtained from the Institute of Biochemistry and Cell Biology (Chinese Academy of Sciences, Shanghai, China). Minimum essential medium (MEM) and Dulbecco's modified Eagle's medium (DMEM), fetal bovine serum (FBS), penicillin, and streptomycin were purchased from Hangzhou Jinuo Biomedical Technology (Hangzhou, China). Water used in all experiments was purified using a Milli-Q Plus 185 water purification system (Millipore, Bedford, MA) with a resistivity higher than 18 M $\Omega$ ·cm. Regenerated cellulose dialysis membranes with a molecular weight cutoff (MWCO) of 14000 or 1000 were acquired from Fisher Scientific (Pittsburgh, PA).

**Synthesis of Gd–Au DENPs-RGD.** The synthesis process of the Gd–Au DENPs-RGD product is illustrated in Figure 1. First, RGD-PEG-COOH segments were synthesized according to protocols described in our previous work with slight modifications.<sup>37</sup> Then G5-NH<sub>2</sub> dendrimers were sequentially reacted with 2,2',2''-(10-(2-((2,5-dioxopyrrolidin-1-yl)oxy)-2-oxoethyl)-1,4,7,10-tetraazacyclododecane-1,4,7-triyl)triacetic acid (DOTA-NHS), RGD-PEG-COOH, and PEG monomethyl ether with the other end of the carboxyl group (mPEG-COOH, MW = 2000) to form the raw product of the G5-NH<sub>2</sub>-DOTA-(PEG-RGD)-mPEG dendrimers according to the procedures described in our previous work with modifications.<sup>6</sup> Subsequently, the raw G5-NH<sub>2</sub>-DOTA-(PEG-RGD)-mPEG dendrimers were used as templates to synthesize Au NPs using protocols described in our previous papers with slight modifications.<sup>39,40</sup> The formed raw product of the {(Au<sup>0</sup>)<sub>200</sub>-G5-NH<sub>2</sub>-DOTA(Gd)-(PEG-RGD)-mPEG} DENPs was subjected to an acetylation reaction to convert the remaining dendrimer terminal amines to acetamide groups according to a procedure described in the literature.<sup>39</sup> Through extensive dialysis and lyophilization processes, the target Gd–Au DENPs-RGD product was obtained. The intermediate products G5-NH<sub>2</sub>-DOTA-(PEG-RGD) and G5-NH<sub>2</sub>-DOTA-(PEG-RGD)-mPEG were also collected and purified to quantify the numbers of RGD and mPEG moieties attached onto each G5 dendrimer.

**Characterization Techniques.** The formed intermediate products, dendrimeric derivatives, and Au DENPs were characterized via <sup>1</sup>H NMR, UV–vis spectroscopy, transmission electron microscopy (TEM), dynamic light scattering (DLS),  $\zeta$  potential, and inductively coupled plasma atomic emission spectroscopy (ICP-AES). The X-ray attenuation property and T<sub>1</sub> relaxometry of the samples were assessed according to protocols described in our previous work.<sup>6</sup>

**Cell Culture.** U87MG cells were continuously cultured and passaged in regular MEM supplemented with 10% heat-

inactivated FBS, 100 U/mL penicillin, and 100 U/mL streptomycin in a 37 °C incubator with 5% CO<sub>2</sub>. The cells cultured in regular medium express high-level  $\alpha_v\beta_3$  integrin, while the cells cultured in regular medium containing 2.5  $\mu$ M free RGD express low-level  $\alpha_v\beta_3$  integrin. Likewise, L1210 cells were also continuously cultured in regular DMEM supplemented with 10% heat-inactivated FBS, 100 U/mL penicillin, and 100 U/mL streptomycin in a 37 °C incubator with 5% CO<sub>2</sub>.

#### In Vitro Cytotoxicity, Hemolysis, and Cellular Uptake

**Assays.** The cytotoxicity of the Gd–Au DENPs-RGD probe was evaluated via 3-(4,5-dimethylthiazol-2-yl)-2,5-diphenyltetrazolium bromide (MTT) colorimetric assay and cell morphology observation. The hemocompatibility of the probe was assessed via a standard hemolysis assay. The cellular uptake of the Gd–Au DENPs-RGD probe was evaluated by ICP-AES. All assays were similar to those described in the literature.<sup>6,10</sup>

**In Vivo Targeted Dual-Mode CT/MR Imaging of a Xenograft Small Tumor Model.** Animal experiments were carried out according to protocols approved by the institutional committee for animal care and also in accordance with the policy of the National Ministry of Health. Male 4–6-week-old BALB/c nude mice (20–22 g, Shanghai Slac Laboratory Animal Center, Shanghai, China) were subcutaneously injected with  $1 \times 10^6$  U87MG cells/mouse in the right side of their oxters. When the tumor nodules reached a volume of 27–64 mm<sup>3</sup> after approximately 2 weeks postinjection, the mice were anesthetized by intraperitoneal injection of 0.3 mL of 3% pentobarbital sodium (12 mL/kg), and the Gd–Au DENPs-RGD probe ([Au] = 0.1 M, 200  $\mu$ L in phosphate-buffered saline (PBS)) was intravenously delivered via the tail vein. For comparison, free RGD (1 mg/mL, 200  $\mu$ L in PBS) was preinjected via the tail vein, and after 30 min, the Gd–Au DENPs-RGD probe ([Au] = 0.1 M, 200  $\mu$ L in PBS) was intravenously injected. CT imaging of the tumor model was performed before injection and at 1, 3, and 20 h postinjection of the particles using a GE LightSpeed VCT clinical imaging system (GE Medical Systems, Milwaukee, WI) at 100 kV and 80 mA and with a slice thickness of 0.625 mm. Images were reconstructed by GE Advantage workstation AW4.4 (GE Medical Systems).

MR imaging was conducted using a 3.0 T Signa HDxt superconducting clinical magnetic resonance system with a custom-built rodent receiver coil (Chenguang Med Tech, Shanghai, China). At each time point for each animal, 2D spin-echo MR images were obtained with a 2 mm slice thickness, a repetition time (TR)/echo time (TE) of 2000/81.9 ms, a  $6 \times 6$  cm field of view (FOV), and a  $256 \times 160$  matrix. MR images were obtained both before and after administration of the particles at time points of 1, 3, and 20 h postinjection. The MR contrast enhancement was quantified by the contrast-to-noise ratio (CNR) using the GE workstation, where the CNR can be calculated by  $[\text{SNR}(\text{signal noise ratio})_a - \text{SNR}_b]/\text{SNR}_b$  according to the literature (a and b indicate the investigated area and the control area).<sup>41,42</sup>

**In Vivo Biodistribution.** The tumor-bearing BALB/c nude mice (20–22 g, Shanghai Slac Laboratory Animal Center, Shanghai, China) were used to analyze the in vivo biodistribution of the Gd–Au DENPs-RGD probe. The mice were euthanized, and the heart, liver, spleen, lung, and kidney organs and the tumor were extracted and weighed after intravenous injection of the Gd–Au DENPs-RGD probe ([Au] = 0.1 M, 200  $\mu$ L in PBS) via the tail vein at different time

points (3, 24, and 120 h postinjection). The organs were digested by aqua regia solution overnight. The Au content in different organs or tumor was quantified by ICP-AES.

**Statistical Analysis.** The one-way analysis of variance (ANOVA) statistical method was performed to evaluate the significance of the experimental data. A value of 0.05 was selected as the significance level, and the data are indicated with one asterisk for  $p < 0.05$ , two asterisks for  $p < 0.01$ , and three asterisks for  $p < 0.001$ . All additional experimental details can be found in the Supporting Information.

## RESULTS AND DISCUSSION

**Synthesis and Characterization of the Gd–Au DENPs-RGD Probe.** Different from our previous study related to the synthesis of FA-targeted Gd–Au DENPs,<sup>6</sup> in this study, G5 dendrimers were used as a platform to sequentially link Gd chelator DOTA-NHS, PEGylated RGD peptide (RGD-PEG-COOH), and mPEG-COOH. Then the functionalized G5 dendrimers were used as templates to synthesize Au NPs. Followed by Gd(III) chelation, a final acetylation step was performed to convert the remaining dendrimer terminal amines to acetamide groups (Figure 1). The use of dendrimers as templates is important because once the formed Au DENPs are delivered to cancer cells, the AuNPs are unlikely to be released from the dendrimers due to the fact that part of the dendrimer terminal amines and tertiary amines are able to strongly interact with the Au particle surface.<sup>39</sup>

DOTA-NHS was first covalently attached to the surface of the G5 dendrimer. According to the established method based on NMR integration reported in our previous work,<sup>6,35</sup> the number of DOTA moieties attached to each G5 dendrimer was estimated to be 8.8.

To render the finally formed particles with improved biocompatibility, increased Au loading capacity for sensitive CT imaging applications,<sup>6,35,40</sup> and simultaneous targeting specificity, RGD-PEG-COOH and mPEG-COOH were sequentially conjugated to the DOTA-modified G5 dendrimers. Thiolated RGD was first linked with 6-maleimidohexanoic acid N-hydroxysuccinimide ester, followed by reaction with the bifunctional NH<sub>2</sub>-PEG-COOH to form the RGD-PEG-COOH segments. Through NMR integration, the number of RGD moieties attached to each PEG was estimated to be 0.9 (Figure S1a, Supporting Information). By analyzing the subsequently formed G5-NH<sub>2</sub>-DOTA-(PEG-RGD) (Figure S1b, Supporting Information) and G5-NH<sub>2</sub>-DOTA-(PEG-RGD)-mPEG (Figure S1c, Supporting Information) dendrimers via <sup>1</sup>H NMR spectroscopy, we can conclude that both RGD-PEG-COOH and mPEG-COOH are successfully conjugated onto the surface of the G5 dendrimer, in agreement with our previous work.<sup>6</sup> By comparison of the NMR peak integration between the PEG and dendrimer –CH<sub>2</sub>– protons, the number of RGD-PEG-COOH and mPEG-COOH moieties attached to each G5 dendrimer was measured to be 7.5 and 9.3, respectively.

The formed G5-NH<sub>2</sub>-DOTA-(PEG-RGD)-mPEG dendrimers were then used as templates to entrap Au NPs and chelate Gd(III) ions, followed by acetylation of the remaining dendrimer terminal amines to diminish the polycationic character of the dendrimers.<sup>6</sup> The formed multifunctional Gd–Au DENPs-RGD probe was characterized via different techniques. The final acetylation modification of the dendrimer terminal amines led to the formation of the nanoprobe with a slightly positive surface potential ( $6.1 \pm 1.9$  mV), in agreement with the literature.<sup>6,10</sup> The composition of the nanoprobe was



analyzed by ICP-AES. The practical Au atom:G5 dendrimer molar ratio was estimated to be 197:1, approximately similar to the initial Au salt/dendrimer molar feeding ratio (200:1), confirming the complete transformation of Au(III) to Au(0). The average number of Gd(III) ions complexed with each NP was estimated to be 26, which is much higher than that of the attached DOTA moieties per dendrimer (8.8) and that of the attached DOTA moieties per G5-Gd-RGD conjugate (control device without Au NPs; 12.0). This may be due to the fact that the entrapped Au NPs within the dendrimer interior strongly interact with Gd(III) ions, resulting in the high payload of Gd within the Gd–Au DENPs-RGD probe, in agreement with our previous work.<sup>35</sup>

TEM was used to characterize the size and morphology of the Gd–Au DENPs-RGD probe (Figure 2). It is clear that the

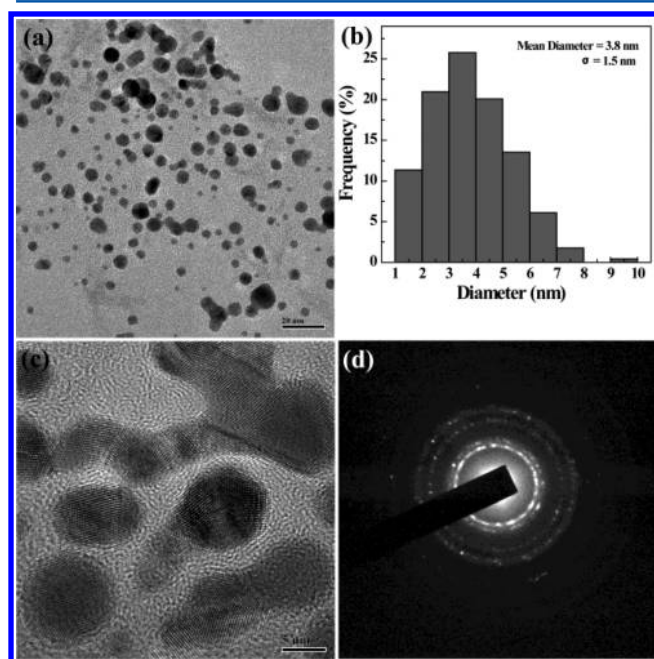


**Figure 2.** TEM image (a), size distribution histogram (b), high-resolution TEM image (c), and selected area electron diffraction pattern (d) of the Gd–Au DENPs-RGD probe.

Au core NPs display a spherical shape (Figure 2a) with a mean diameter of 3.8 nm and with a narrow size distribution (Figure 2b). The Au core NPs are highly crystalline as lattices can be clearly seen in a typical high-resolution TEM image (Figure 2c), and the measured regular lattice spacing of 0.24 nm corresponds to the Au(111) plane. Likewise, the (111), (200), (220), and (311) rings in the selected area electron diffraction (SAED) pattern clearly indicate the face-centered-cubic (fcc) crystal structure of the Au core NPs (Figure 2d). The hydrodynamic size of the Gd–Au DENPs-RGD probe was measured by DLS to be  $71.7 \pm 0.8$  nm (Figure S2, Supporting Information), which is slightly smaller than that of the control device without RGD ( $89.4 \pm 0.6$  nm) reported in our previous study.<sup>35</sup> This may be due to the fact that the modification of RGD-PEG-COOH affords the formed Gd–Au DENPs-RGD probe with slightly different aggregation behaviors in aqueous solution when compared to the control device modified with mPEG-COOH.

**Stability of the Gd–Au DENPs-RGD Probe.** The stability of the Gd–Au DENPs-RGD probe is an important issue that

should be addressed before its biomedical applications. UV–vis spectroscopy was used to investigate the stability of the Gd–Au DENPs-RGD probe under different pH and temperature conditions (Figure S3, Supporting Information). This is because the aggregation state of Au NPs can be readily reflected by the change of their characteristic surface plasmon resonance (SPR) band in the UV–vis spectrum.<sup>43</sup> It can be seen that the UV–vis spectrum of Gd–Au DENPs-RGD dissolved in water under different pH values (5–8) does not have any appreciable changes, suggesting that the formed Gd–Au DENPs-RGD probe is stable in the studied pH range. In addition, the UV–vis spectrum of Gd–Au DENPs-RGD does not show any obvious changes in aqueous solution under different temperatures (4, 25, 37, and 50 °C, respectively), suggesting a good stability of the probe in a temperature range of 4–50 °C. Finally, the stability of the Gd–Au DENPs-RGD probe was also assessed by exposing it to PBS and cell culture medium at 4 °C. We show that no precipitation occurs even after the probe is stored for a period of one month (Figure S4, Supporting Information). Taken together, our results show that the developed Gd–Au DENPs-RGD probe is not only stable under the studied pH and temperature conditions, but also stable in different aqueous media, which is important for its biomedical imaging applications.

#### X-ray Attenuation Property and $T_1$ MR Relaxometry.

We next investigated the X-ray attenuation property and  $T_1$  MR relaxometry of the Gd–Au DENPs-RGD probe. Due to the higher atomic number of Au than that of iodine, which is the radiodense element of conventional CT contrast agents (e.g., Omnipaque), Au NPs have been frequently utilized as a novel contrast agent for CT imaging applications.<sup>44,45</sup> CT phantom images of the aqueous solutions of the Gd–Au DENPs-RGD probe show that with the Au concentration the brightness of the CT images increases (Figure 3a). By plotting the

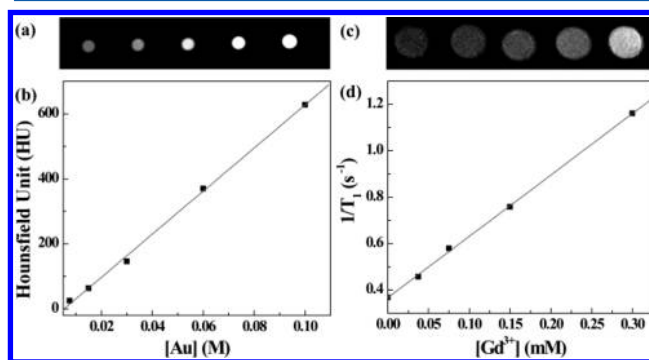


**Figure 3.** CT images (a) and X-ray attenuation (Hounsfield unit, HU) intensity (b) of Gd–Au DENPs-RGD at different Au concentrations. (c) and (d) show the  $T_1$  MR phantom images and the linear fitting of the inverse  $T_1$  of Gd–Au DENPs-RGD as a function of the Gd concentration.

attenuation intensity of the probe as a function of the Au concentration, a linear curve was observed (Figure 3b). It can be seen that the attenuation intensity of the Gd–Au DENPs-RGD probe increases with the Au concentration, in agreement with our previous studies.<sup>6,35,40</sup> This suggests that the developed Gd–Au DENPs-RGD probe can be potentially used for CT imaging applications.

To explore the potential to use the Gd–Au DENPs-RGD probe for  $T_1$ -weighted MR imaging,  $T_1$  relaxometry of the probe was performed. It can be seen that the  $T_1$ -weighted MR

images of the aqueous solution of the probe become brighter and brighter with the Gd concentration (Figure 3c). By plotting the inverse  $T_1$  as a function of the Gd concentration, a linear curve was obtained with a slope of  $2.643 \text{ mM}^{-1} \text{ s}^{-1}$  (Figure 3d), which can be defined to be the longitudinal relaxivity ( $r_1$ ) of the probe. Compared with the other Gd–Au DENPs reported in the literature,<sup>6,35</sup> the  $r_1$  relaxivity of the Gd–Au DENPs-RGD probe is larger than that of Gd–Au DENPs ( $1.05 \text{ mM}^{-1} \text{ s}^{-1}$ ), but smaller than that of Gd–Au DENPs-FA ( $3.139 \text{ mM}^{-1} \text{ s}^{-1}$ ), thereby offering slightly different MR imaging sensitivities. The X-ray attenuation property and  $r_1$  relaxivity of the Gd–Au DENPs-RGD probe are quite comparable to those of the nontargeted Gd–Au DENPs reported in our previous work,<sup>35</sup> thus rendering the formed Gd–Au DENPs-RGD probe with great potential for dual-mode CT/MR imaging applications.

**Cytotoxicity and Hemolysis Assays.** Prior to the biomedical imaging applications, it is essential to assess the cytocompatibility and hemocompatibility of the Gd–Au DENPs-RGD probe. The in vitro cytotoxicity of the probe was tested by MTT viability assay of U87MG cells (Figure 4a).

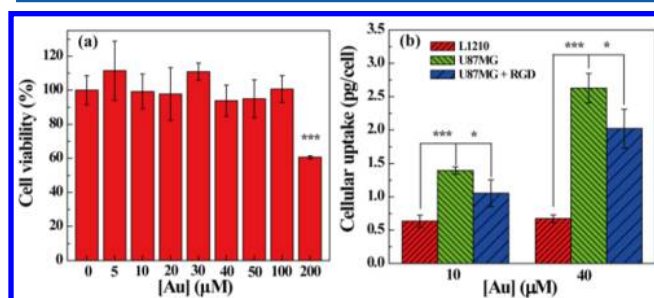


**Figure 4.** (a) MTT viability assay of U87MG cells treated with Gd–Au DENPs-RGD at different Au concentrations for 24 h. (b) Cellular uptake of Au in U87MG and L1210 cells treated with the Gd–Au DENPs-RGD probe at different Au concentrations for 3 h. For comparison, U87MG cells pretreated with free RGD (2.5  $\mu\text{M}$ ) for 1 h were also tested under similar experimental conditions. Data are represented as the mean  $\pm$  SD ( $n = 3$ ).

It can be seen that the viability of U87MG cells incubated with the Gd–Au DENPs-RGD probe at a Au concentration up to 100  $\mu\text{M}$  does not display apparent changes when compared with the control cells treated with PBS. At the tested highest Au concentration of 200  $\mu\text{M}$ , the cell viability is still higher than 60%. This suggests that the developed Gd–Au DENPs-RGD probe is cytocompatible in the Au concentration range of 0–100  $\mu\text{M}$ , in agreement with our previous work.<sup>6</sup>

The cytocompatibility of the Gd–Au DENPs-RGD probe was further confirmed by phase contrast microscopic observation of the morphology of U87MG cells (Figure S5, Supporting Information). Clearly, the cells treated with the probe at Au concentrations of 5–100  $\mu\text{M}$  appear to be normal and healthy and display the same morphology as the control cells treated with PBS. However, at a Au concentration of 200  $\mu\text{M}$ , a portion of the cells become rounded and nonadherent, indicating cell death. The cell morphology observation results corroborate the above MTT assay data, indicating that the Gd–Au DENPs-RGD probe is cytocompatible in the Au concentration range of 0–100  $\mu\text{M}$ . It should be noted that, compared to the nonspecific Gd–Au DENPs<sup>35</sup> and FA-targeted Gd–Au DENPs<sup>6</sup> reported in our previous work, the cytocompatibility of the probe follows the order Gd–Au DENPs-FA > Gd–Au DENPs-RGD > Gd–Au DENPs

according to the cytotoxicity test. Although the tested cell lines are different, it is generally believed that the modification of FA or RGD moieties onto the surface of the NPs is able to render them with improved cytocompatibility.

Hemolysis assay was used to test the hemocompatibility of the Gd–Au DENPs-RGD probe (Figure S6, Supporting Information). In contrast to the positive control of water that displays an apparent hemolysis effect, at a tested Au concentration up to 108 mM, the probe does not exhibit an appreciable hemolysis effect when compared to the negative control of PBS (Figure S6a). The hemolysis percentage (HP) of the probe at different Au concentrations was further quantified (Figure S6b). We show that, under the studied Au concentrations, the HP of the Gd–Au DENPs-RGD probe is less than the threshold value of 5%.<sup>10</sup> These results suggest that the developed Gd–Au DENPs-RGD probe is pretty hemocompatible in the studied Au concentration range.

**In Vitro Cellular Uptake of the Gd–Au DENPs-RGD Probe.** To confirm the RGD-mediated targeting specificity of the Gd–Au DENPs-RGD probe to  $\alpha_v\beta_3$  integrin-overexpressing cancer cells, ICP-AES was used to quantify the cellular Au uptake (Figure 4b). Compared to the control L1210 cells without  $\alpha_v\beta_3$  integrin expression,<sup>36,46</sup> the Au uptake in U87MG cells was 2.2 and 3.9 times higher at Au concentrations of 10 and 40 mM, respectively. Furthermore, the U87MG cells preincubated with free RGD peptide display much less Au uptake than the regular U87MG cells at Au concentrations of 10 and 40 mM, respectively ( $p < 0.05$ ). This is due to the fact that the incubation of free RGD peptide is able to block the  $\alpha_v\beta_3$  integrin expression on the cell surface,<sup>47</sup> thereby leading to suppressed Au uptake. These results suggest that the Gd–Au DENPs-RGD probe can specifically target  $\alpha_v\beta_3$  integrin-expressing cancer cells in a receptor-mediated manner, which is essential for them to be used for targeted CT/MR dual-modality imaging of  $\alpha_v\beta_3$  integrin-expressing cancer cells.

**In Vivo Targeted Dual-Mode CT/MR Imaging of a Tumor Model.** With the good cytocompatibility, hemocompatibility, and targeting specificity of the Gd–Au DENPs-RGD probe, we next explored the feasibility to use it for in vivo targeted dual-mode CT/MR imaging of a tumor model. Due to the fact that early noninvasive detection and characterization of solid tumors is a fundamental prerequisite for effective therapeutic intervention,<sup>29,48</sup> we established a nascent small xenografted U87MG tumor model. CT imaging of the tumor-bearing mice was performed (Figure 5), and the CT value of the tumor region was quantified before injection and at different time points post intravenous injection (Figure 6a). An obvious CT contrast enhancement in the tumor region can be seen at 1, 3, and 20 h postinjection of the probe when compared with before injection. At 20 h postinjection, the CT value of the tumor region starts to descend, suggesting that the nanoprobe is able to be metabolized with the time post-injection. The RGD-mediated targeting specificity was confirmed by preinjection of free RGD, which is believed to block the  $\alpha_v\beta_3$  integrin expression in the tumor region.<sup>49</sup> Apparently, the tumor region of mice treated with free RGD displays much less CT contrast enhancement than that of the mice without treatment with free RGD at different time points postinjection. In particular, the  $\Delta\text{HU}$  ( $(\text{HU}_{\text{after probe injection}} - \text{HU}_{\text{before probe injection}})/\text{HU}_{\text{before probe injection}}$ ) of the tumor injected with the Gd–Au DENPs-RGD probe was calculated to be 90.7%, which is twice that of the tumor preinjected with free



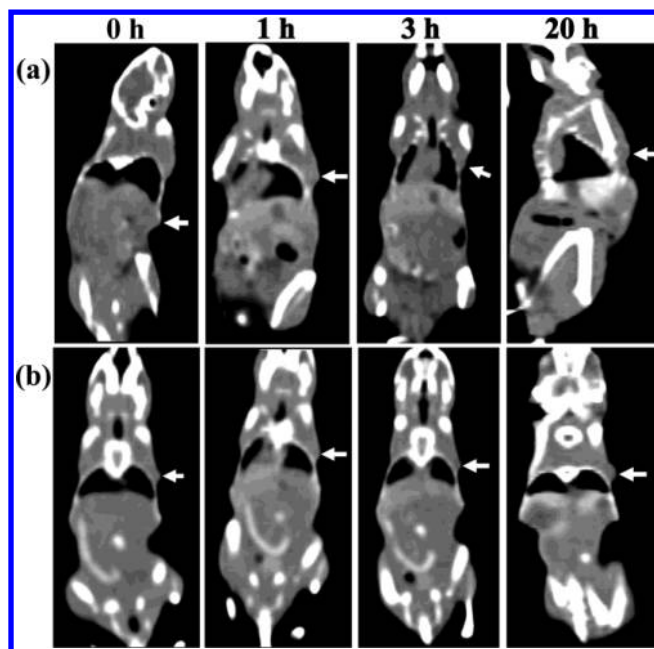


**Figure 5.** Representative transection CT images of mice bearing transplanted nascent U87MG tumors after intravenous injection of the Gd–Au DENPs–RGD probe (a). Control mice were preinjected with free RGD (1 mg/mL, 200  $\mu$ L in PBS), and after 30 min, the mice were injected with the Gd–Au DENPs–RGD probe (b). Images were taken before (0 h) and at 1, 3, and 20 h postinjection of the probe. The white arrow indicates the tumor region.

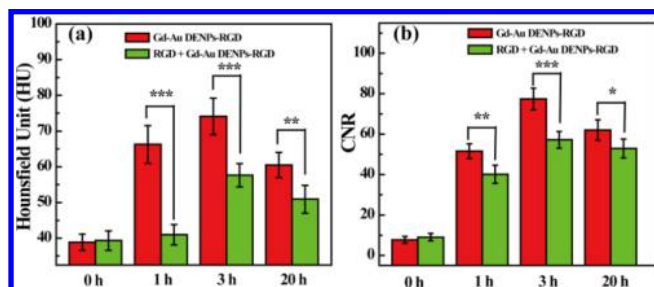


**Figure 6.** (a) CT values (Hounsfield unit, HU) of the tumor region at different time points. (b) CNR of the tumor region in  $T_1$ -weighted MR images at different time points. The mice were intravenously injected with the Gd–Au DENPs–RGD probe ([Au] = 0.1 M, 200  $\mu$ L in PBS) via the tail vein.

RGD at 3 h postinjection of the probe (Figure S7a, Supporting Information).

On the other hand, the loaded Gd(III) ions within the probe also enabled  $T_1$ -weighted MR imaging of the tumor model (Figure 7). The tumor region became brighter and the tumor margin was able to be clearly observed with the time postinjection of the probe. Similar to the CT imaging results, the tumor MR CNR is increased significantly at different time points postinjection when compared with before injection (Figure 6b). In addition, preinjection of free RGD is able to weaken the tumor MR signal intensity when compared with the tumor mice without pretreatment of free RGD at the same time points. This further confirmed the RGD peptide-mediated targeting role that leads to specifically enhanced MR contrast enhancement in the tumor region. Quantitative MR signal intensity measurements show that the  $\Delta\text{CNR}$  ( $(\text{CNR}_{\text{after probe injection}} - \text{CNR}_{\text{before probe injection}})/$

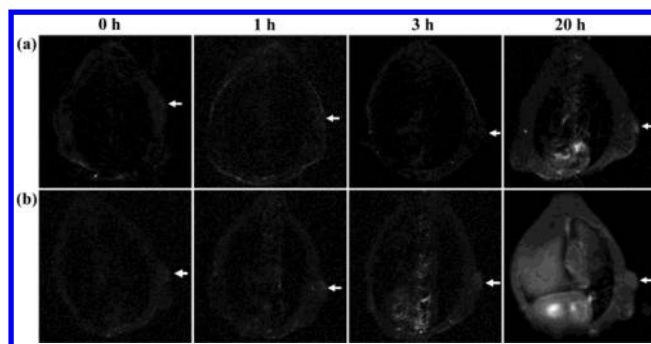


**Figure 7.** Representative transection  $T_1$ -weighted MR images of mice bearing transplanted nascent U87MG tumors (a). Control mice were preinjected with free RGD (1 mg/mL, 200  $\mu$ L in PBS), and after 30 min, the mice were injected with the Gd–Au DENPs–RGD probe (b). Images were taken before (0 h) and at 1, 3, and 20 h postinjection of the Gd–Au DENPs–RGD probe ([Au] = 0.1 M, 200  $\mu$ L in PBS). The white arrow indicates the tumor region.

$\text{CNR}_{\text{before probe injection}}$ ) of the tumor injected with the probe is 921.1%, 1.7 times higher than that pretreated with free RGD, followed by injection of the probe at 3 h postinjection (Figure S7b, Supporting Information). The MR imaging results are consistent with those of the CT imaging.

**In Vivo Biodistribution of the Gd–Au DENPs–RGD Probe.** For in vivo biomedical imaging applications, it is important to understand the in vivo biodistribution behavior of the Gd–Au DENPs–RGD probe. ICP–AES results (Figure S8, Supporting Information) reveal that, at 3, 24, and 120 h postinjection, the liver and spleen have a significant Au uptake, with Au uptake of 1335.1  $\mu\text{g/g}$  (3 h), 1214.0  $\mu\text{g/g}$  (24 h), and 1227.3  $\mu\text{g/g}$  (120 h) in the liver and 930.1  $\mu\text{g/g}$  (3 h), 608.3  $\mu\text{g/g}$  (24 h), and 1276.2  $\mu\text{g/g}$  (120 h) in the spleen, demonstrating that the Gd–Au DENPs–RGD probe is able to be recognized by the reticuloendothelial system (RES).<sup>50</sup> However, a significant portion of particles seem to be able to escape from the RES in the liver and spleen and be accumulated in the other organs (such as the lung, kidney, and heart) and tumor. The tumor uptake of Au rapidly approaches 45.0  $\mu\text{g/g}$  at 3 h postinjection, thereby enabling effective dual-mode CT/MR imaging of the tumor region. Then the tumor Au uptake gradually declines with the time postinjection. These results were consistent with those measured by CT and MR imaging.

## CONCLUSION

In summary, a dendrimer-based multifunctional RGD-targeted nanoprobe was developed for targeted dual-modality CT/MR imaging of tumors. The versatile dendrimer nanotechnology enabled effective entrapment of Au NPs within the dendrimer interior and covalent conjugation of Gd chelator on the dendrimer periphery to complex Gd(III) ions. The formed Gd–Au DENPs–RGD probe is water dispersible, colloidal stable at different pH and temperature conditions, non-cytotoxic, and hemocompatible in the given concentration range. Importantly, with the coexistence of Au NPs and Gd(III) ions and the RGD modification, the developed Gd–Au DENPs–RGD probe enabled targeted dual-modality CT/MR imaging of a xenograft tumor model overexpressing  $\alpha_v\beta_3$  integrin in vivo through the RGD-mediated active targeting pathway. The developed RGD-modified multifunctional dendrimeric nanoprobe may hold great promise to be used

for targeted dual-mode CT/MR imaging of different types of  $\alpha_v\beta_3$  integrin-overexpressing tumors.

## ■ ASSOCIATED CONTENT

### ■ Supporting Information

Additional experimental details, materials characterization, and in vitro and in vivo experimental data. This material is available free of charge via the Internet at <http://pubs.acs.org>.

## ■ AUTHOR INFORMATION

### Corresponding Authors

\*E-mail: [mingwu\\_shen@yahoo.com](mailto:mingwu_shen@yahoo.com).

\*E-mail: [guixiangzhang@sina.com](mailto:guixiangzhang@sina.com).

\*E-mail: [xshi@dhu.edu.cn](mailto:xshi@dhu.edu.cn).

### Author Contributions

\*Q.C. and H.W. contributed equally to this work.

### Notes

The authors declare no competing financial interest.

## ■ ACKNOWLEDGMENTS

This research is financially supported by the National Natural Science Foundation of China (Grants 21273032, 81341050, 81271384, 81270032, and 81401458), the Program for New Century Excellent Talents in University, State Education Ministry, and the Program for Professor of Special Appointment (Eastern Scholar) at Shanghai Institutions of Higher Learning. H.W. thanks the Shanghai Pujiang Program (Grant 13PJD026) and the Key Program of Science and Technology Commission of Shanghai Municipality (Grant 13NM1401700) for financial support. C.P. thanks the Shanghai Natural Science Foundation (Grant 14ZR1432400) for support. X.S. gratefully acknowledges the Fundação para a Ciência e a Tecnologia (FCT) and Santander bank for the Invited Chair in Nanotechnology and the FCT for funding through Project PTDC/CTM-NAN/1748/2012 and through Strategic Plan PEst-OE/QUI/UI0674/2011.

## ■ REFERENCES

- (1) Qiao, Z.; Shi, X. *Prog. Polym. Sci.* **2014**, DOI: 10.1016/j.progpolymsci.2014.1008.1002.
- (2) Ametamey, S. M.; Honer, M.; Schubiger, P. A. *Chem. Rev.* **2008**, *108*, 1501–1516.
- (3) Louie, A. *Chem. Rev.* **2010**, *110*, 3146–3195.
- (4) Lusic, H.; Grinstaff, M. W. *Chem. Rev.* **2012**, *113*, 1641–1666.
- (5) Gao, W.; Ji, L.; Li, L.; Cui, G.; Xu, K.; Li, P.; Tang, B. *Biomaterials* **2012**, *33*, 3710–3718.
- (6) Chen, Q.; Li, K.; Wen, S.; Liu, H.; Peng, C.; Cai, H.; Shen, M.; Zhang, G.; Shi, X. *Biomaterials* **2013**, *34*, 5200–5209.
- (7) Kim, D.; Park, S.; Lee, J. H.; Jeong, Y. Y.; Jon, S. *J. Am. Chem. Soc.* **2007**, *129*, 7661–7665.
- (8) Liu, H.; Xu, Y.; Wen, S.; Chen, Q.; Zheng, L.; Shen, M.; Zhao, J.; Zhang, G.; Shi, X. *Chem.—Eur. J.* **2013**, *19*, 6409–6416.
- (9) Liu, H.; Xu, Y.; Wen, S.; Zhu, J.; Zheng, L.; Shen, M.; Zhao, J.; Zhang, G.; Shi, X. *Polym. Chem.* **2013**, *4*, 1788–1795.
- (10) Peng, C.; Li, K.; Cao, X.; Xiao, T.; Hou, W.; Zheng, L.; Guo, R.; Shen, M.; Zhang, G.; Shi, X. *Nanoscale* **2012**, *4*, 6768–6778.
- (11) Popovtzer, R.; Agrawal, A.; Kotov, N. A.; Popovtzer, A.; Balter, J.; Carey, T. E.; Kopelman, R. *Nano Lett.* **2008**, *8*, 4593–4596.
- (12) Fang, Y.; Peng, C.; Guo, R.; Zheng, L.; Qin, J.; Zhou, B.; Shen, M.; Lu, X.; Zhang, G.; Shi, X. *Analyst* **2013**, *138*, 3172–3180.
- (13) Rabin, O.; Manuel Perez, J.; Grimm, J.; Wojtkiewicz, G.; Weissleder, R. *Nat. Mater.* **2006**, *5*, 118–122.
- (14) Oh, M. H.; Lee, N.; Kim, H.; Park, S. P.; Piao, Y.; Lee, J.; Jun, S. W.; Moon, W. K.; Choi, S. H.; Hyeon, T. *J. Am. Chem. Soc.* **2011**, *133*, 5508–5515.
- (15) He, M.; Huang, P.; Zhang, C.; Hu, H.; Bao, C.; Gao, G.; He, R.; Cui, D. *Adv. Funct. Mater.* **2011**, *21*, 4470–4477.
- (16) Li, J.; He, Y.; Sun, W.; Luo, Y.; Cai, H.; Pan, Y.; Shen, M.; Xia, J.; Shi, X. *Biomaterials* **2014**, *25*, 3666–3677.
- (17) Li, J.; Zheng, L.; Cai, H.; Sun, W.; Shen, M.; Zhang, G.; Shi, X. *Biomaterials* **2013**, *34*, 8382–8392.
- (18) Shi, X.; Wang, S. H.; Swanson, S. D.; Ge, S.; Cao, Z.; Van Antwerp, M. E.; Landmark, K. J.; Baker, J. R., Jr. *Adv. Mater.* **2008**, *20*, 1671–1678.
- (19) Wen, S.; Zhao, Q.; An, X.; Zhu, J.; Hou, W.; Li, K.; Huang, Y.; Shen, M.; Zhu, W.; Shi, X. *Adv. Healthcare Mater.* **2014**, *3*, 1568–1577.
- (20) Swanson, S. D.; Kukowska-Latallo, J. F.; Patri, A. K.; Chen, C.; Ge, S.; Cao, Z.; Kotlyar, A.; East, A. T.; Baker, J. R., Jr. *Int. J. Nanomed.* **2008**, *3*, 201–210.
- (21) Cai, H.; An, X.; Cui, J.; Li, J.; Wen, S.; Li, K.; Shen, M.; Zheng, L.; Zhang, G.; Shi, X. *ACS Appl. Mater. Interfaces* **2013**, *5*, 1722–1731.
- (22) Li, J.; Shi, X.; Shen, M. *Part. Part. Syst. Charact.* **2014**, *31*, 1223–1237.
- (23) Wang, S. H.; Shi, X.; Van Antwerp, M.; Cao, Z.; Swanson, S. D.; Bi, X.; Baker, J. R., Jr. *Adv. Funct. Mater.* **2007**, *17*, 3043–3050.
- (24) Chou, S. W.; Shau, Y. H.; Wu, P. C.; Yang, Y. S.; Shieh, D. B.; Chen, C. C. *J. Am. Chem. Soc.* **2010**, *132*, 13270–13278.
- (25) Xiao, Q.; Bu, W.; Ren, Q.; Zhang, S.; Xing, H.; Chen, F.; Li, M.; Zheng, X.; Hua, Y.; Zhou, L. *Biomaterials* **2012**, *33*, 7530–7539.
- (26) Lee, N.; Cho, H. R.; Oh, M. H.; Lee, S. H.; Kim, K.; Kim, B. H.; Shin, K.; Ahn, T.-Y.; Choi, J. W.; Kim, Y.-W.; Choi, S. H.; Hyeon, T. *J. Am. Chem. Soc.* **2012**, *134*, 10309–10312.
- (27) Pagel, M. D. *Nanomedicine* **2011**, *6*, 945–948.
- (28) Jennings, L. E.; Long, N. J. *Chem. Commun.* **2009**, 3511–3524.
- (29) Kobayashi, H.; Longmire, M. R.; Ogawa, M.; Choyke, P. L.; Kawamoto, S. *Lancet Oncol.* **2010**, *11*, 589–595.
- (30) Alric, C.; Taleb, J.; Duc, G. L.; Mandon, C.; Billotey, C.; Meur-Herland, A. L.; Brochard, T.; Vocanson, F.; Janier, M.; Perriat, P. *J. Am. Chem. Soc.* **2008**, *130*, 5908–5915.
- (31) Park, J.-A.; Kim, H.-K.; Kim, J.-H.; Jeong, S.-W.; Jung, J.-C.; Lee, G.-H.; Lee, J.; Chang, Y.; Kim, T.-J. *Bioorg. Med. Chem. Lett.* **2010**, *20*, 2287–2291.
- (32) Regino, C. A. S.; Walbridge, S.; Bernardo, M.; Wong, K. J.; Johnson, D.; Lonser, R.; Oldfield, E. H.; Choyke, P. L.; Brechbiel, M. W. *Contrast Media Mol. Imaging* **2008**, *3*, 2–8.
- (33) Dong, W.; Li, Y.; Niu, D.; Ma, Z.; Liu, X.; Gu, J.; Zhao, W.; Zheng, Y.; Shi, J. *Small* **2013**, *9*, 2500–2508.
- (34) Xiao, Q.; Zheng, X.; Bu, W.; Ge, W.; Zhang, S.; Chen, F.; Xing, H.; Ren, Q.; Fan, W.; Zhao, K.; Hua, Y.; Shi, J. *J. Am. Chem. Soc.* **2013**, *135*, 13041–13048.
- (35) Wen, S.; Li, K.; Cai, H.; Chen, Q.; Shen, M.; Huang, Y.; Peng, C.; Hou, W.; Zhu, M.; Zhang, G. *Biomaterials* **2013**, *34*, 1570–1580.
- (36) Shukla, R.; Thomas, T. P.; Peters, J.; Kotlyar, A.; Myc, A.; Baker, J. R., Jr. *Chem. Commun.* **2005**, 5739–5741.
- (37) He, X.; Alves, C.; Oliveira, N.; Rodrigues, J.; Zhu, J.; Bányai, I.; Tomás, H.; Shi, X. *Colloids Surf., B* **2015**, *125*, 82–89.
- (38) Santos, J. L.; Pandita, D.; Rodrigues, J.; Pêgo, A. P.; Granja, P. L.; Balian, G.; Tomás, H. *Mol. Pharmaceutics* **2010**, *7*, 763–774.
- (39) Shi, X.; Wang, S.; Meshinchi, S.; Van Antwerp, M. E.; Bi, X.; Lee, I.; Baker, J. R., Jr. *Small* **2007**, *3*, 1245–1252.
- (40) Peng, C.; Zheng, L.; Chen, Q.; Shen, M.; Guo, R.; Wang, H.; Cao, X.; Zhang, G.; Shi, X. *Biomaterials* **2012**, *33*, 1107–1119.
- (41) Krazinski, A. W.; Meinel, F. G.; Schoepf, U. J.; Silverman, J. R.; Canstein, C.; De Cecco, C. N.; Geyer, L. L. *Eur. Radiol.* **2014**, *24*, 2677–2684.
- (42) Liu, X.; Zhang, N.; Fan, Z.; Feng, F.; Yang, Q.; Zheng, H.; Liu, P.; Li, D. *J. Magn. Reson. Imaging* **2014**, *40*, 1422–1429.
- (43) Ghosh, S. K.; Pal, T. *Chem. Rev.* **2007**, *107*, 4797–4862.
- (44) Hayashi, K.; Nakamura, M.; Ishimura, K. *Adv. Healthcare Mater.* **2013**, *2*, 756–763.



- (45) Wang, L.; Xing, H.; Zhang, S.; Ren, Q.; Pan, L.; Zhang, K.; Bu, W.; Zheng, X.; Zhou, L.; Peng, W. *Biomaterials* **2013**, *34*, 3390–3401.
- (46) Shukla, R.; Hill, E.; Shi, X.; Kim, J.; Muniz, M. C.; Sun, K.; Baker, J. R., Jr. *Soft Matter* **2008**, *4*, 2160–2163.
- (47) Zhu, S.; Qian, L.; Hong, M.; Zhang, L.; Pei, Y.; Jiang, Y. *Adv. Mater.* **2011**, *23*, H84–H89.
- (48) Zhang, C.; Xie, X.; Liang, S.; Li, M.; Liu, Y.; Gu, H. *Nanomed.: Nanotechnol., Biol. Med.* **2012**, *8*, 996–1006.
- (49) Li, Z.; Jin, Q.; Huang, C.; Dasa, S.; Chen, L.; Yap, L.-p.; Liu, S.; Cai, H.; Park, R.; Conti, P. S. *Theranostics* **2011**, *1*, 371–380.
- (50) Liu, Z.; Cai, W.; He, L.; Nakayama, N.; Chen, K.; Sun, X.; Chen, X.; Dai, H. *Nat. Nanotechnol.* **2007**, *2*, 47–52.